

Research Article

Influence of Milling Time on Structural and Microstructural Parameters of Ni₅₀Ti₅₀ Prepared by Mechanical Alloying Using Rietveld Analysis

E. Sakher ^{1,2}, N. Loudjani,³ M. Benchiheb,² and M. Bououdina ⁴

¹Laboratoire de Physique des Solides, Department of Physics, Faculty of Science, University Badji Mokhtar, Annaba, Algeria

²Laboratoire d'Elaboration et d'Analyse des Matériaux LEAM, Department of Physics, Faculty of Science, University Badji Mokhtar, Annaba, Algeria

³Laboratoire de Microstructures et Defauts, Department of Physics, Faculty of Science, University of Mentouri, Constantine, Algeria

⁴Department of Physics, College of Science, University of Bahrain, P.O. Box 32038, Manama, Bahrain

Correspondence should be addressed to E. Sakher; elfahem.sakher@univ-annaba.org

Received 16 September 2017; Accepted 5 December 2017; Published 14 January 2018

Academic Editor: Leszek A. Dobrzański

Copyright © 2018 E. Sakher et al. This is an open access article distributed under the Creative Commons Attribution License, which permits unrestricted use, distribution, and reproduction in any medium, provided the original work is properly cited.

Nanostructured Ni₅₀Ti₅₀ powders were prepared by mechanical alloying from elemental Ni and Ti micrometer-sized powders, using a planetary ball mill type Fritsch Pulverisette 7. In this study, the effect of milling time on the evolution of structural and microstructural parameters is investigated. Through Rietveld refinements of X-ray diffraction patterns, phase composition and structural/microstructural parameters such as lattice parameters, average crystallite size $\langle L \rangle$, microstrain $\langle \epsilon^2 \rangle^{1/2}$, and stacking faults probability (SFP) in the frame of MAUD software have been obtained. For prolonged milling time, a mixture of amorphous phase, NiTi-martensite (B19'), and NiTi-austenite (B2) phases, in addition to FCC-Ni(Ti) and HCP-Ti(Ni) solid solutions, is formed. The crystallite size decreases to the nanometer scale while the internal strain increases. It is observed that, for longer milling time, plastic deformations introduce a large amount of stacking faults in HCP-Ti(Ni) rather than in FCC-Ni(Ti), which are mainly responsible for the observed large amount of the amorphous phase.

1. Introduction

NiTi-based shape memory alloys have attracted great scientific and technological interests, due to their remarkable mechanical and chemical properties, such as superelasticity, shape memory behavior, good corrosion resistance [1, 2], hydrogen storage ability, and good biocompatibility [3, 4]; thereby they are very appropriate for biomedical and dentistry applications [5, 6]. The observed shape memory effect in NiTi alloy is mainly caused by the existence of NiTi-austenite (B2) and NiTi-martensite (B19') phases [7].

Numerous methods have been used to synthesize nanocrystalline shape memory alloys (NSMAs), including ion-milling deposition [8], melt-spinning [9], high-pressure torsion [10], and sol-gel technique [11]. Meanwhile, physical techniques for producing NiTi intermetallic compound using

elemental Ni and Ti powders [12] have been reported such as conventional powder metallurgy [13], self-propagating high temperature synthesis [14], explosive shock-wave compression [15], and mechanical alloying (MA) [16].

Among the above-cited methods, mechanical alloying (MA) was found to be very effective in the synthesis of Ni₅₀Ti₅₀-based nanocrystalline alloys or nanostructured powders. Through this technique, a large variety of materials are produced such as intermetallics, extended solid solutions, quasicrystals, and amorphous phases [17]. Moreover, in this process, the reduction of particle size is observed, resulting in ultra-fine grained or nanocrystalline materials. Because of the very fine grain size, nanocrystalline materials exhibit diverse and interesting properties, which are different and often considerably improved in comparison with conventional coarse-grained polycrystalline materials [18]. MA of Ni₅₀Ti₅₀

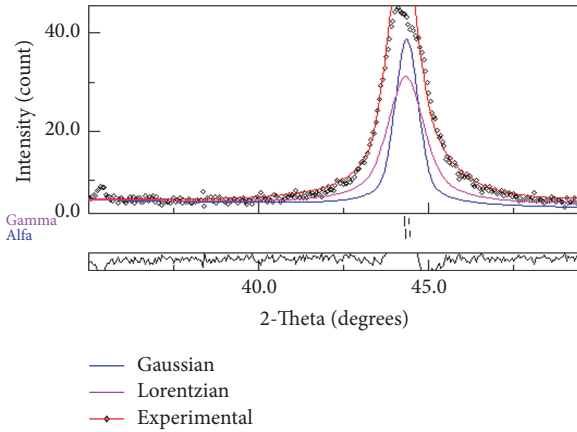


FIGURE 1: The illustration of Gaussian and Lorentzian peak-shape functions.

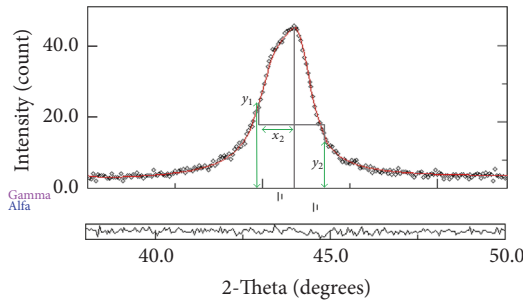


FIGURE 2: The schematic illustration of the asymmetric diffraction peak.

elemental powders mixture can lead to amorphous phase, nanocrystalline solid solution [12], NiTi-austenite (B2), and NiTi-martensite (B19') phase [19].

Moreover, it is very important to characterize the powders obtained by MA in terms of phase composition in addition to structural and microstructural features. The crystallite size and microstrain in powdered particles can be determined through X-ray diffraction peak broadening. Herein, it is worth mentioning that the shape of peak can be described as a combination of two functions: Gaussian associated with microstrain and Lorentzian associated with crystallite size (Figures 1, 2, and 3) [20, 21]. Meanwhile, instrumental parameters have to be taken into consideration. Numerous models, like Williamson-Hall [22], Halder-Wagner [23], Warren-Averbach [24], and Rietveld method [25], have been widely used for the determination of structural and microstructural parameters.

The Rietveld analysis, a full-pattern fitting of X-ray diffraction patterns, has been reported as a powerful method for structural and microstructural characterization [26], including qualitative and quantitative phase analyses of multiphase nanocrystalline materials containing significant number of overlapping reflections [27]. In the literature, Rietveld's method was successfully adopted for the determination of microstructural parameters of various systems [28–30].

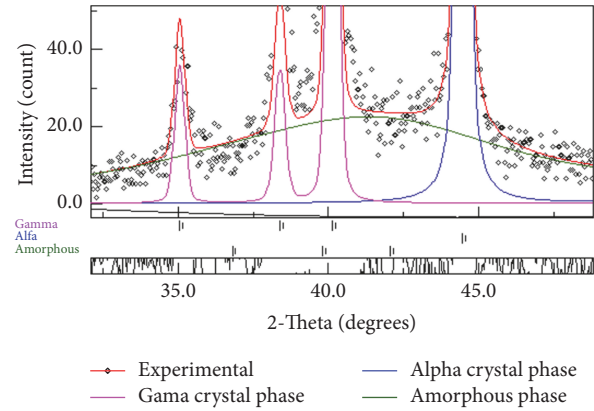


FIGURE 3: Contribution of crystalline and amorphous phases to an XRD pattern.

The aim of this research work is devoted to the investigation of milling time on structural and microstructural modifications occurring in mechanically alloyed Ni₅₀Ti₅₀ powder mixture. In-depth analysis using the Rietveld method of X-ray data is carried out, in terms of phase composition, crystallite size, microstrain, lattice parameter, and lattice defects such as dislocation density and stacking faults.

2. Experimental Part

2.1. Mechanical Alloying of Ni₅₀Ti₅₀ Powder Mixture. High purity elemental Ti (~150 μm, 99.97%) and Ni (~45 μm, 99.99%) powders (Aldrich) were mixed in appropriate proportions in order to obtain the Ni₅₀Ti₅₀ (at.%) composition. MA was performed under argon atmosphere using Fritsch Pulverisette 7 planetary ball mill equipped with hardened steel vial (80 mL) and balls (15 mm diameter). The disk speed rotation was $\Omega = 400$ rpm. The ball-to-powder mass ratio was 23 : 1. To avoid excessive temperature increase, a milling time pause of 30 min was applied after each hour of milling. The powders were milled for several periods of time, that is, 0, 1, 3, 6, 24, 48, and 72 h.

2.2. Characterization. The milled powders were examined by X-ray diffraction (XRD) method, using X-ray Philips X, Pert diffractometer equipped with Cu-K_α radiation source ($\lambda_{Cu} = 0.15418$ nm). The phase analysis was performed by using ICDD (PDF-2, 2012) files. Both structural and microstructural parameters were determined from the refinements of XRD patterns using MAUD program (version 2.55) based on the Rietveld method [31].

Using the Rietveld refinement and Warren-Averbach method [24, 25] in the frame of MAUD software [31], a detailed analysis of XRD profiles can be performed leading to the determination of phase composition in addition to structural and microstructural parameters for each phase, such as lattice parameters (a, b, c), the average crystallite size $\langle L \rangle$, microstrain $\langle \epsilon^2 \rangle^{1/2}$, and stacking fault probabilities (SFP).

The Rietveld method consists of simulating a pattern from simulated crystallographic model that is as close as possible to the measured pattern, which depends on analytical functions in order to characterize the microstructure of powders and determine $\langle L \rangle$, $\langle \epsilon^2 \rangle^{1/2}$, and SFP.

The structural refinement method uses the minimization technique of least squares making it possible to approach the experimental pattern from a starting structural model. The minimized function, or residue, is written:

$$M = \sum_i w_i \cdot (y_i - y_{ic})^2, \quad (1)$$

where y_i and y_{ic} are, respectively, the observed and calculated intensities; w_i is the weight associated with the intensity y_i . For refinements by least square method, w_i is taken equal to $1/y_i$.

From a structural model, each contribution y_{ci} is obtained by the combination of different Bragg contributions and continuous background:

$$y_{ci} = y_{bi} + \sum_k I_k \phi_k, \quad (2)$$

where I_k is the integrated intensity of the reflection, ϕ_k is the profile shape function, and y_{bi} a polynomial function fitting the background.

The integrated intensity of the reflection is calculated according to certain structural and geometric parameters:

$$I = S_c |F_k|^2 m_k \frac{(L_p)}{(V_c)^2}, \quad (3)$$

where S_c is the scale factor, F_k is the structure factor inclusive of Debye-Waller factor and site occupancy, m_k is the multiplicity of (hkl) reflection, L_p is the usual Lorentz-polarization factor, and V_c is the cell volume.

The profile shape function is the result of the convolution of instrumental and sample broadenings:

$$\phi_k = \phi^S \otimes \phi^I, \quad (4)$$

where ϕ^S is the sample broadening and ϕ^I is the instrumental broadening. The latter can be written as follows:

$$\phi^I = S \otimes A, \quad (5)$$

where S and A are, respectively, the symmetric and asymmetric components of the instrumental profile, determined for particular geometry of the diffractometer. The asymmetric component is given by

$$A = \exp[-a_s |2\theta - 2\theta_0| \tan(2\theta_0)], \quad (6)$$

where a_s is the asymmetry parameter and θ_0 is the Bragg angle of $K_{\alpha 1}$ peak.

The Pseudo-Voigt function is defined as the contribution of a pure Lorentzian and a pure Gaussian (which will be corrected for the asymmetry of the peaks):

$$pV(2\theta_i) = \sum I_{nt} [\eta L(2\theta_i) + (1 - \eta) G(2\theta_i)], \quad (7)$$

where I_{nt} is the scale parameter of the pV function, η is the Gaussianity of X-ray peaks, and $L(2\theta_i)$ and $G(2\theta_i)$ are Gaussian and Lorentzian components, respectively:

$$G(2\theta_i) = I_0 \exp \left[-\ln 2 \left(\frac{2\theta - 2\theta_0}{\text{FWHM}} \right)^2 \right], \quad (8)$$

$$L(2\theta_i) = I_0 \left[1 + \left(\frac{2\theta - 2\theta_0}{\text{FWHM}} \right)^2 \right]^{-n} \quad n = 1; 1.5; 2,$$

where $2\theta_0$ is peak position, I_0 is the peak intensity, and FWHM is the full-width at half-maximum of reflections.

The FWHM is given by the Caglioti formula [32]:

$$\text{FWHM} = \sqrt{U \cdot \tan^2 \theta + V \cdot \tan \theta + W} \quad (9)$$

where U , V , and W are coefficients of quadratic polynomial or the coefficients of Caglioti.

The sample broadening ϕ^S is the convolution of broadening due to the finite size of crystallites $\langle L \rangle$, the r.m.s microstrain $\langle \epsilon^2 \rangle^{1/2}$, and planar defects expressed in terms of stacking faults probability (SFP):

$$\text{SFP} = [1.5(\alpha' + \alpha'') + \beta], \quad (10)$$

where α' , α'' are the intrinsic and extrinsic deformation faults, respectively, and β is the twin faults.

The Delft model for sample broadening gives the integral breadths for the Gaussian and Lorentzian components:

$$\beta_G = 4 \langle \epsilon^2 \rangle^{1/2} \tan \theta \quad (11)$$

$$\beta_L = \frac{\lambda}{L_{\text{eff}} \cos \theta}.$$

L_{eff} is an effective size computed from the crystallite size $\langle L \rangle$ and λ is the radiation wavelength.

The MAUD software is based on the Rietveld method combined with a Fourier analysis. The detailed analysis was performed considering Fourier coefficients A_L ; after Stoke's corrections the size coefficients A_L^S and distortion coefficients A_L^D , which are related to A_L in the following equation:

$$A_L = A_L^D A_L^S, \quad (12)$$

were separated from the log plot of A_L with the square root of the quadratic sum of the Miller indices h_0^2 where [33]

$$h_0^2 = h^2 + k^2 + l^2. \quad (13)$$

The reflections affected by stacking faults correspond to peaks satisfying the conditions:

$$h + k + l \neq 3n \quad (n \text{ is an integer}) \text{ for FCC structure} \quad (14)$$

$$h - k \neq 3n \quad (l \text{ even or odd}) \text{ for HCP structure.}$$

The microstructural parameters like effective size, L_{eff} , and the r.m.s. microstrain $\langle \epsilon^2 \rangle^{1/2}$ are related, respectively, to the initial slope of A_L^S with L and slope of $\log A_L$ with h_0^2 :

$$-\left(\frac{dA_L^S}{dL}\right)_{L \rightarrow 0} = \frac{1}{L_{\text{eff}}}, \quad (15)$$

$$A_L^D = \exp\left(\frac{-2\pi^2 L^2 \langle \epsilon^2 \rangle^{1/2} h_0^2}{a^2}\right),$$

where L denotes a normal length to the reflecting planes.

The SFP like intrinsic α' , extrinsic α'' , and deformation twin fault probability β were evaluated through the following relation:

$$\frac{1}{L_{\text{eff}}} = \frac{1}{L} + \frac{1.5(\alpha' + \alpha'') + \beta}{ah_0(u+b)} \sum_b |\pm L_0|, \quad (16)$$

where a is the lattice parameter, u is unbroadened by faulting, b is the number of reflections broadened, and L_0 is the third coordinate replacing (hkl) indices ($L_0 = h + k + l$) [33].

Peak asymmetry is obtained by measuring the intensity value on either side of the peak at two positions which are equidistant from the peak center (y_1 and y_2) and derived from the extrinsic deformation and twin faulting probabilities. The mathematical expression for asymmetry is evaluated as follows:

$$y_2 - y_1 = \frac{2A(4.5\alpha'' + \beta)}{c_2 x_2 \sqrt{3}\pi(u+b)} \sum (\pm) \frac{L_0}{|L_0|}, \quad (17)$$

where the coefficient c_2 depends on the peak $2\theta_0$ position:

$$c_2 = 1 + \left\{ \frac{\lambda}{4\pi L_{\text{eff}} [\sin(\theta_0 - x_2) - \sin\theta_0]} \right\}^2, \quad (18)$$

where A is the area of the peak, y_1 is the peak intensity in the diffraction angle $(\theta_0 + x_2)$, and θ_0 is the completely symmetrical profile center [31].

The peak shift can be written, in terms of intrinsic and extrinsic deformation faulting probability, as follows [33]:

$$\Delta(2\theta)^\circ = \frac{90\sqrt{3}(\alpha' + \alpha'') \tan\theta}{\pi^2 h_0^2 (u+b)} \sum_b (\pm L_0). \quad (19)$$

From the values of lattice parameters, crystallite size, and microstrain, the dislocations density (ρ) can be calculated using the following formula:

$$\rho = 2\sqrt{3} \frac{\langle \epsilon^2 \rangle^{1/2}}{\langle L \rangle B_v}, \quad (20)$$

where B_v is Burgers vector, which is equal to $a\sqrt{6}/3$ for the hexagonal close-packed (HCP) structure and $a\sqrt{2}/2$ for the face-centered cubic (FCC) structure.

The calculated profile yields scaling factors for each phase to fit the intensity of the observed pattern. These scale factors

are related to the respective relative weight fractions by the following equation [34]:

$$W_i = \frac{S_i (ZMV)_i}{\sum_{k=1}^n S_k (ZMV)_k}, \quad (21)$$

where Z is the number of formula units in the unit cell, M is the molecular mass of the formula unit, V is the unit cell volume, S is the Rietveld scale factor, and W_i is the weight fraction of phase i : the index “ k ” in the summation covering all phases that are included in the model [34].

The standard procedure is to determine the amorphous fraction by the internal standard method. The amount of the amorphous phase is obtained as the complement to one of the total amounts of crystalline phases [31]. The weight percentage of the amorphous phase in a sample can be given by the following relationship [35]:

$$W_a = \frac{1}{1 - W_S} \left(1 - \frac{W_S}{W_R}\right), \quad (22)$$

where W_a is the amorphous fraction, W_S is the weighted internal standard fraction, and W_R is the refined fraction of the internal standard.

After adjusting the parameters of the instrument, the peak positions are corrected by successive refinements to eliminate systematic errors by taking into account the errors of the angular offset ($\Delta 2\theta$) and the displacement of the sample. The background is adjusted by a polynomial of degree (2 to 5), for the first milling time. On the other hand, for longer milling times, the increase in the intensity of the background requires the use of higher degree polynomials. Then, the parameters of the crystal structure are refined, namely, the crystal parameters, the atomic positions, the Debye-Waller factor, and the percentage of phases. In the last step, we proceed to the refinement of crystallite size $\langle L \rangle$, microstrain $\langle \epsilon^2 \rangle^{1/2}$, and the probability of all three types of planes defects α' , α'' , and β .

To evaluate the refinement, several factors have been introduced in order to know the agreement between calculated and observed models [34].

The minimization was carried out by using the reliability index parameter, R_{wp} (weighted residual error), and R_{exp} (the expected error) defined as follows [27]:

$$R_{wp} = \left[\frac{\sum_{i=1}^N (y_i - y_{ic})^2}{\sum_{i=1}^N y_i (2\theta_i)} \right]^{1/2}, \quad (23)$$

$$R_{\text{exp}} = \left[\frac{N - P}{\sum_{i=1}^N y_i (2\theta_i)} \right]^{1/2},$$

where N and P are the number of experimental points and the number of fitting parameters, respectively.

It is possible to calculate a statistical parameter, which must tend towards the unity for a successful refinement; the goodness of fit “ χ^2 ” is defined as the ratio between R_{wp} and R_{exp} :

$$\chi^2 = \frac{R_{wp}}{R_{\text{exp}}}. \quad (24)$$

The profile refinements continue until convergence is reached; the value of the quality factor χ^2 (GOF) is approaching one.

3. Results and Discussion

3.1. Structural Analysis. The X-ray diffraction (XRD) patterns of $\text{Ni}_{50}\text{Ti}_{50}$ powders (0, 1, 3, 6, 12, 24, 48, and 72 h), shown in Figure 4, clearly indicate that MA introduces significant changes. There is a gradual peaks' broadening with a decrease in peaks' intensity as a function of the milling time, demonstrating the great impact of milling on the crushed starting elemental Ni and Ti starting powders, which can be associated with several processes occurring progressively [36]:

- (i) particles (grains) refinement (reduction of crystallite size);
- (ii) introduction of crystalline defects (interstices, dislocations, and grain boundaries);
- (iii) increase in the rate of microdeformations (large amount of energy);
- (iv) fragmentation of crystallites and/or effect of atomic disorder.

The as-mentioned phenomena result from welding and disordering effects, occurring because of repeated collisions (ball-powder-ball and ball-powder-wall of bowl).

The overlapping of XRD reflections arising from different phases results in an enlargement of peaks' width accompanied with a slight shift towards lower angles, indicating a slight increase in interatomic distances leading to unit cell expansion.

After few hours of milling, one can see the appearance of halo around $35\text{--}50^\circ$, which overlaps with reflections belonging to HCP-Ti and FCC-Ni. This can be attributed to the formation of an amorphous phase, which is explained by the significant structural disorder induced by the severe plastic deformations occurring during milling process.

Figure 5 shows the refined XRD patterns for elemental Ni and Ti powders, based on initial structural models: (i) face-centered cubic (FCC) for Ni with lattice parameter $a = 0.3524$ nm; (ii) hexagonal close-packed (HCP) for Ti with lattice parameters $a = 0.2952$ nm and $c = 0.4686$ nm. All the results are reported in Table 1.

The best Rietveld refinements of XRD patterns (1, 3, and 6 h) were obtained with three components: FCC-Ni, HCP-Ti, and an amorphous phase (Figures 6(a), 6(b), and 6(c)). The nanometer scaled diffusion couples are produced by high energy mechanical milling which involves fracture and cold-welding of milled powders. Thus, the atomic diffusivity is improved through the creation of a large amount of structural defects. As a result, metastable phases may form at early stage of the milling by solid-state reaction (SSR) process.

After 12 h of milling, the diffraction peaks of elemental FCC-Ni, HCP-Ti, and the amorphous phase remain while new diffraction peaks related to NiTi-martensitic (Figure 6(d)) emerge.

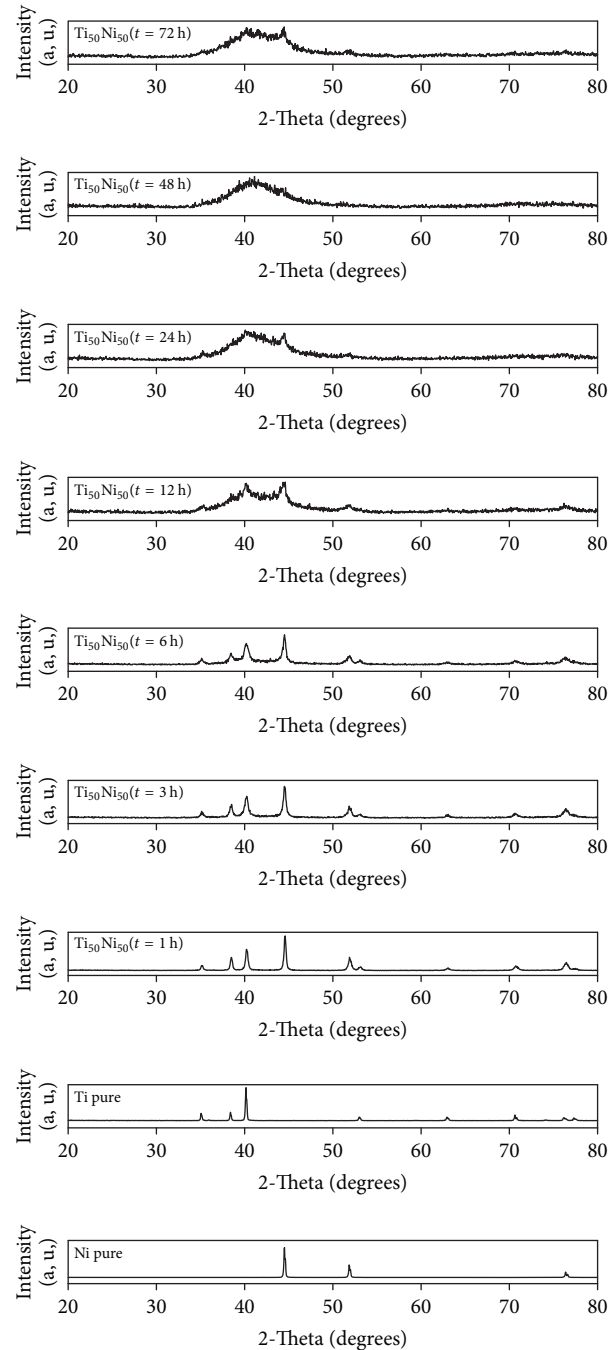
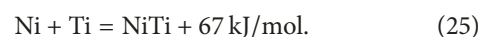


FIGURE 4: XRD patterns of the $\text{Ni}_{50}\text{Ti}_{50}$ powders at different milling time.

Further milling up to (24 h), leads to a complete disappearance of HCP-Ti peaks associated with the formation of NiTi-austenitic (Figure 6(e)), while Ni-SS remains present with small amount (15.38%). Furthermore, it is well-known that the crystallite size decreases with the increase of negative mixing enthalpy (ΔH) [36]. In addition, NiTi phase could be the product of the reaction between Ni and Ti due to their negative mixing enthalpy ($\Delta H = -67$ kJ/mol) [37, 38]:



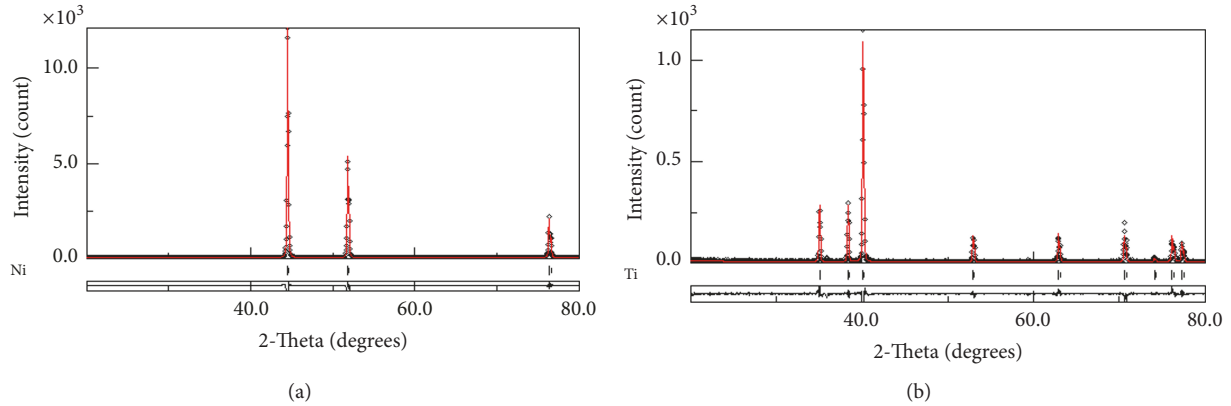


FIGURE 5: Rietveld refinements for XRD pattern of (a) Ni (GOF = 1.54) and (b) Ti (GOF = 1.11).

TABLE 1: Structural and microstructural properties of unmilled Ni and Ti using the Rietveld refinements.

Microstructural properties	Element	
	Nickel (Ni)	Titanium (Ti)
Crystal structure	FCC	HCP
Space group	Fm-3m	P63/mmc
Cell parameters (nm)	$a = 0.3524$	$a = 0.2952$ $b = 0.4686$
Atom positions	$x: 3.65141 \cdot 10^{-4}$ $y: -8.8563 \cdot 10^{-5}$ $z: -5.9118 \cdot 10^{-5}$	$x: 0.3333$ $y: 0.6667$ $z: 0.2500$
Occupancy	1.0001	1.0000
Crystallite size (nm)	318.4175	241.2283
Microstrain (%)	$3.1758 \cdot 10^{-4}$	$4.5954 \cdot 10^{-4}$
Stacking faults probability (SFP) (%)	$1.5832 \cdot 10^{-4}$	0.1744
Dislocations density ($\times 10^{16} \text{ m}^{-2}$)	0.0014	0.0027

Beyond 48 h of milling, XRD patterns reveal the same phases, NiTi-austenite (B2) and NiTi-martensite (B19'), but with the dominance of the amorphous phase (Figures 6(f) and 6(g)) having a relative proportion of about 89.24%.

In order to investigate the phase's stabilities during mechanical milling, we calculated the phase proportions of the identified phases as a function of milling time. The results obtained are shown in Figure 7. Accordingly, the milling process was divided into four main stages (I, II, III, and IV) as shown in Figure 7.

In the first stage I (0-1 h), a decrease in the proportions of Ti and Ni was observed, which may be due to the mutual diffusion and to the formation of amorphous phase and solid solutions FCC-Ni (Ti) and HCP-Ti (Ni).

During the second stage II (1-12 h), which represents a postformation of amorphous phase, we note that Ti-SS and Ni-SS ratios decrease inversely to the proportion of the amorphous phase.

Then, in the third stage III (12-24 h), the percentage of initial Ni-SS continues to decrease, meanwhile Ti-SS has disappeared completely, thus leading to the continuous increase in the amount of the amorphous phase and the formation of martensitic phase. The formation of martensitic phase may

be due to the negative mixing enthalpy [37]. The complete transformation of the severely deformed phases into an amorphous structure is achieved upon further milling, through the mechanically enhanced solid-state amorphisation, which requires the existence of chemical disordering, point defects, vacancies, interstitials, lattice defects, and dislocations.

The fourth and final stage IV (24-72 h) is characterized by the emergence of new NiTi-austenite phase, while the initial Ni-SS entirely disappears favoring also to the formation of NiTi-austenite. The continuous increase in the proportion of the amorphous phase can be explained evidently along with the reduction in the amount of NiTi-martensite.

After 48 h, the fraction of the amorphous phase decreases due to its crystallization into more stable crystalline phases (NiTi-austenite and NiTi-martensite), which may be attributed to strain energy and the temperature increase during MA due to severe plastic deformations as reported by Amini et al. [19]. However, the amorphous phase is predominant with a relative proportion of about 89.23%.

Indeed, the heavily plastic deformations induce strong distortion of the unit cell structures hence becoming less crystalline. The powdered particles are subjected to continuous defects that lead to a gradual change in the free energy

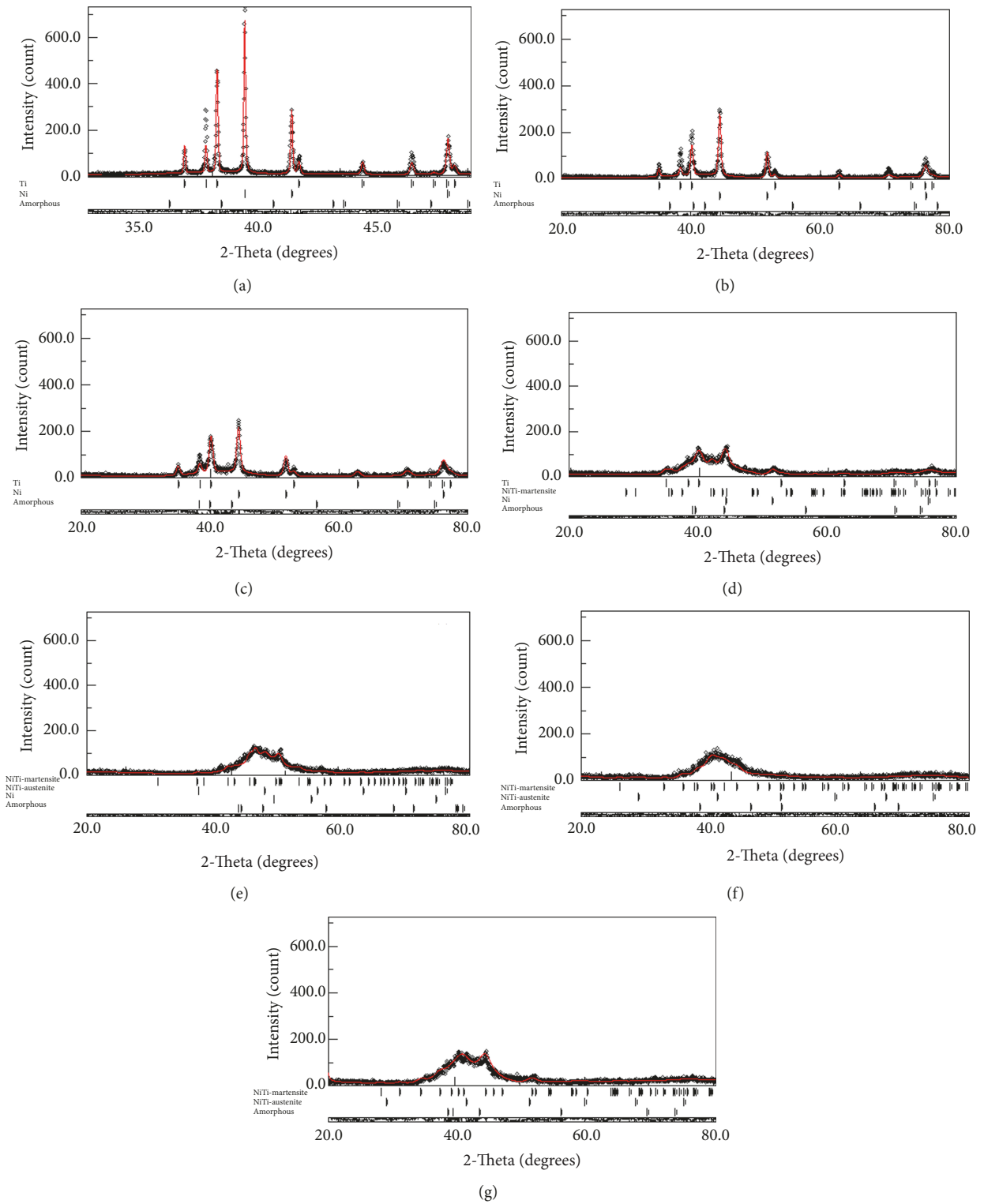


FIGURE 6: Rietveld refinements of XRD patterns of the milled powders for (a) 1 h (GOF = 1.41), (b) 3 h (GOF = 1.45), (c) 6 h (GOF = 1.43), (d) 12 h (GOF = 1.22), (e) 24 h (GOF = 1.20), (f) 48 h (GOF = 1.19), and (g) 72 h (GOF = 1.23).

TABLE 2: Lattice parameters of Ni, Ti, NiTi-austenite, and NiTi-martensite as function of milling time.

Milling time (h)	Ni		Ti	NiTi-austenite	NiTi-martensite		
	<i>a</i> (nm)	<i>a</i> (nm)	<i>b</i> (nm)	<i>a</i> (nm)	<i>a</i> (nm)	<i>b</i> (nm)	<i>c</i> (nm)
0	0.3524	0.2952	0.4686	/	/	/	/
1	0.3519	0.2947	0.4677	/	/	/	/
3	0.3527	0.2953	0.4687	/	/	/	/
6	0.3534	0.2956	0.4687	/	/	/	/
12	0.3560	0.2979	0.4708	/	0.4780	0.4225	0.2978
24	0.3574	/	/	0.3045	0.4134	0.4576	0.2953
48	/	/	/	0.3155	0.4858	0.5110	0.2798
72	/	/	/	0.3134	0.4687	0.4238	0.2942

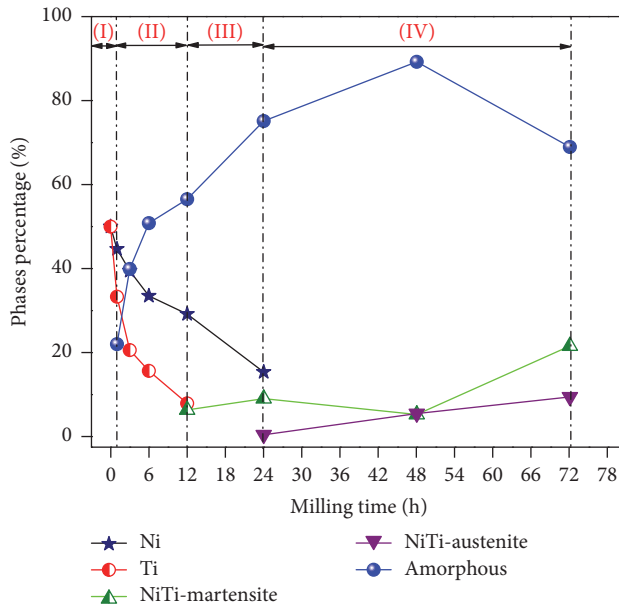


FIGURE 7: Evolution of the proportions of the identified phases as a function of milling time.

of the crystalline phases compared to the amorphous phase resulting into disorder in atomic arrangement.

3.2. Crystallite Size and Microstrain. A diffraction peak broadening, observed with increasing milling time, is usually associated with grain size reduction and increase of internal strain. The variation in the average crystallite size $\langle L \rangle$ and microstrain $\langle \epsilon^2 \rangle^{1/2}$ obtained from Rietveld refinements is plotted as a function of milling time in Figure 8.

In the early stage of milling, one can observe an important decrease of the crystallite size reaching 7 nm (24 h) and 29 nm (12 h) for Ni-SS and Ti-SS, respectively. It is also evident that the reduction in Ni-SS crystallite size is faster than Ti-SS, which is probably related to its smaller initial particle size of Ni ($<45 \mu\text{m}$) compared to Ti ($<150 \mu\text{m}$) [38].

But in the second stage, after 24 h, the crystallite size becomes less dependent on the milling time. This can be explained by the fact that mechanical energy delivered during milling is not sufficient to plastically deform the two phases

NiTi-austenite and NiTi-martensite. The average crystallite size of NiTi-martensite after 72 h is of about 19 nm while that of NiTi-austenite reaches 42 nm (Figure 8(a)). The reduction in crystallite size is mainly due to severe deformations of powders during the milling, as well as the increase in probability of nucleation sites during crystallization, provided by higher defects density [36].

The as-obtained values of the crystallite size are in good agreement with the values previously reported on binary alloys prepared by MA [20, 28, 29].

From Figure 8(b), it is clear that the internal microstrain $\langle \epsilon^2 \rangle^{1/2}$ increases with increasing milling time. Thus during the first stage of milling, $\langle \epsilon^2 \rangle^{1/2}$ of Ni-SS and Ti-SS reaches about 0.7% and 1.16% after 12 h, respectively. The increase of the microstrain can be due to the increase of dislocations density induced by severe plastic deformations [28]. For NiTi-martensite, $\langle \epsilon^2 \rangle^{1/2}$ increases to about 0.9%, after 48 h, and then decreases; this behavior may be explained by the fact that, beyond this time, the crystallite size reaches a stationary value.

It is important to mention that NiTi-austenite is characterized by higher microstrain comparatively to NiTi-martensite, which may be due to a high concentration of stacking faults and a high dislocations density. In fact, actually, the austenite phase is metastable at room temperature and becomes unstable when an external mechanical or thermal energy is introduced. Generally, the values of microstrain achieved during milling for similar systems are around 1.5% [18].

3.3. Lattice Parameters. Table 2 shows the variation of lattice parameters of Ni, Ti, NiTi-austenite, and NiTi-martensite for each milling time as obtained from Rietveld analysis. The decrease of the lattice parameters of Ni and Ti after 1 h of milling is probably due to the compressive forces caused by collisions [27], and therefore reducing the distance between neighboring atoms. It can be noticed that Ni and Ti lattice parameters increase with milling time reaching 0.3574 nm, after 24 h, and $a = 0.2979$ nm and $b = 0.4708$ nm, after 12 h of milling, respectively. This can be attributed to the severe plastic deformations and accumulation of large amount of structural defects such as stacking faults, grain boundaries, and enhanced dislocations density during the milling process [23].

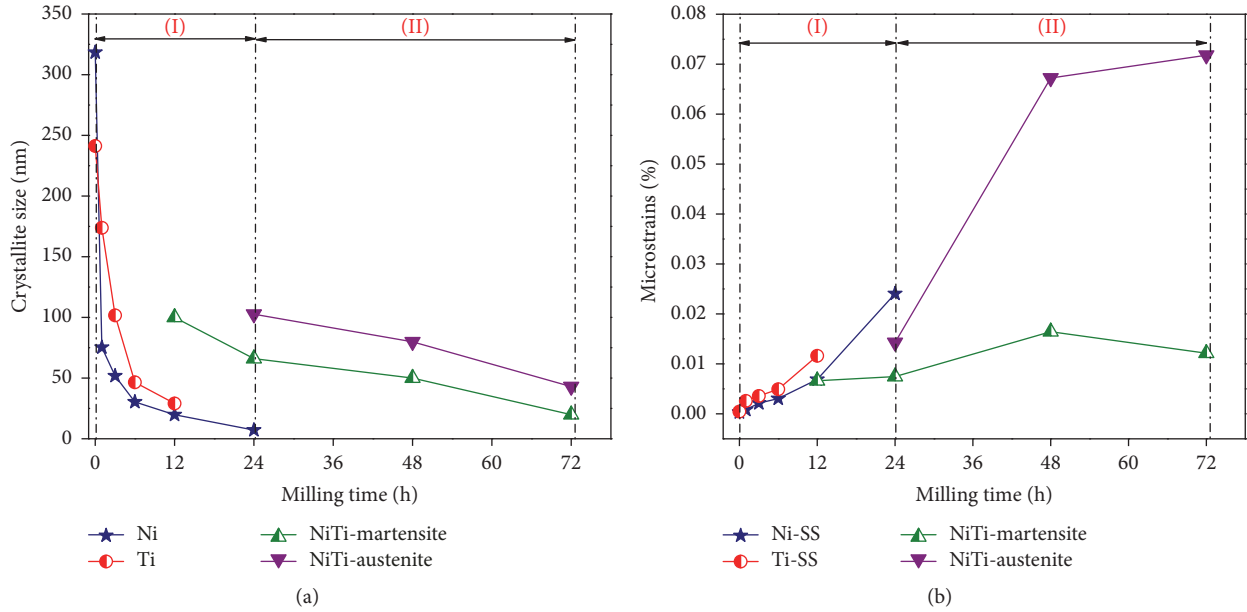


FIGURE 8: Evolution of (a) average crystallite size $\langle L \rangle$ and (b) microstrain $\langle \epsilon^2 \rangle^{1/2}$ as a function of milling time.

For the austenite phase, the lattice parameter increases up to 48 h and then remains nearly stationary until 72 h where it reaches a value of 0.3134 nm. The relative deviation of the lattice parameter ($\Delta a/a_0$) of the austenite phase after 48 hours of milling is 3.96% which is high compared to the relative deviation of the lattice parameter of martensitic phase $\Delta a/a_0 = 1.397\%$, $\Delta b/b_0 = 0.663\%$, and $\Delta c/c_0 = 1.962\%$. This relatively high value can be associated with the severe plastic deformations, which introduces different types of defects such as dislocations, grain boundaries, gaps, and stacking faults and it can be also explained by the formation of a nonstoichiometric composition of the austenite phase.

3.4. Dislocations Density. The variation of the dislocations density can be associated with the ball-to-powder mass ratio that characterizes the collision number, the energy impact, and the number of defects introduced within the lattice.

Figure 9 illustrates the evolution of dislocations density of Ni and Ti as a function of milling time and can be divided into two stages: ρ_I (0–12 h) and ρ_{II} (12–24 h). It is obvious that ρ increases slightly in the first stage ρ_I from about 0.0014×10^{16} to $0.4791 \times 10^{16} \text{ m}^{-2}$ for Ni-SS and $0.0027 \times 10^{16} \text{ m}^{-2}$ to $0.5691 \times 10^{16} \text{ m}^{-2}$ for Ti-SS. The as-obtained ρ values are comparable to the values of dislocations density limit in metals achieved by plastic deformations (10^{13} m^{-2} for screw dislocations and 10^{16} m^{-2} for edge dislocations) [39]. During the final stage ρ_{II} , for Ni-SS, the dislocations density increases considerably up to $2.6851 \times 10^{16} \text{ m}^{-2}$ with the disappearance of Ti. This increase as compared to the first stage ρ_I , could be due to the formation of NiTi-martensite phase. Indeed, the Ti radius is slightly larger than that of Ni ($R_{\text{Ti}} = 0.176 \text{ nm} > R_{\text{Ni}} = 0.149 \text{ nm}$), so the diffusion of Ti into Ni leads to the distortion of Ni crystal structure and hence further increase in the dislocations density. The as-obtained values of the

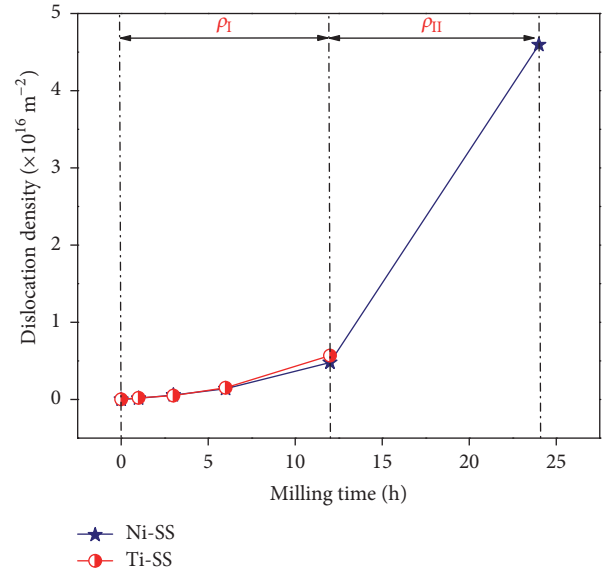


FIGURE 9: Evolution of dislocations density of Ni and Ti as a function of milling time.

dislocations density in the present work are comparable to the values observed in the binary $\text{Co}_{50}\text{Ni}_{50}$ alloy synthesized by high energy ball milling [28].

3.5. Stacking Faults. Heavy deformations introduce stacking faults along (111) planes in FCC metals and alloys. Stacking faults can also be introduced in the basal (0001) or prismatic (10 $\bar{1}$ 0) planes of the hexagonal close backed alloys. These faults can cause anomalous (hkl) dependent peak broadening in the X-ray diffraction patterns [18].

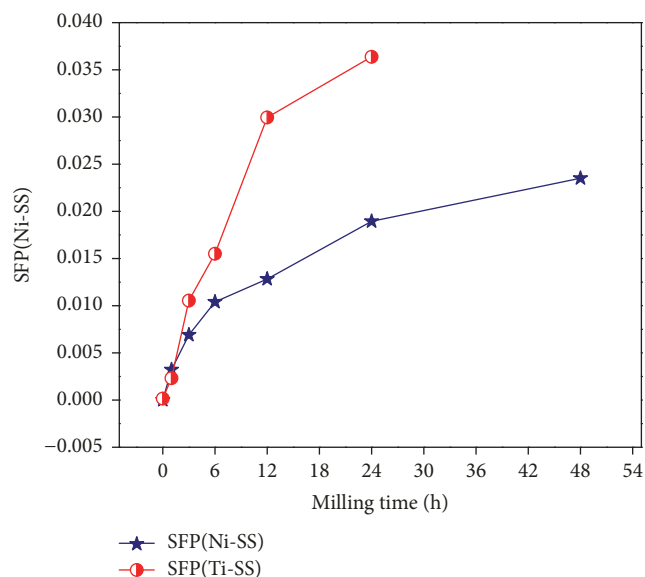


FIGURE 10: Evolution of stacking fault probability for Ni and Ti as a function of milling time.

Figure 10 shows the variation of stacking faults probability (SFP) of HCP-Ti and FCC-Ni as deduced from the Rietveld refinements of XRD patterns of Ni and Ti. In both Ni and Ti crystal structures, two different types of stacking faults can be found, namely, deformation and twin stacking faults. It can be noticed that, for both HCP-Ti and Ni-FCC, SFP increases with increasing milling time; reaching after 24 h a higher value of 0.0364 (HCP-Ti) compared to 0.0189 (FCC-Ni). The increase of SFP for both Ni and Ti with extensive milling time reflects an important increase in the dislocations density (Figure 9). It has been noticed that twinning and deformation stress depend on the initial crystallite size and milling intensity [18].

The parameter $1/(sfp)$ indicates the average number of compacted layers between two stacking faults, either deformation or twin-type, according to Warren's formulae [40]. In fact, there are 27 and 43 ordered planes between the two consecutive stacking faults in HCP-Ti and FCC-Ni after 24 and 48 h of milling, respectively. As it is clear, the values of the average number of compacted layers between two stacking faults in HCP-Ti(Ni) are found to be higher compared to FCC-Ni(Ti) and thus can explain that Ti facilitates the formation of the amorphous phase more than Ni. Meanwhile, Ni contributes to the formation of martensitic and austenitic phases.

4. Conclusion

A mixture of Ni and Ti elemental powders with a nominal composition $Ni_{50}Ti_{50}$ was mechanically alloyed in a planetary ball mill under argon atmosphere. The final products were nanocrystalline NiTi-martensite (B19) and NiTi-austenite (B2) phases with an average crystallite size in the range of a few nanometers (19 nm~42 nm) with a large internal strain (1.02%~1.48%) and a dominant amorphous phase (89 wt.%).

The induced heavy plastic deformations lead to crystallite size refinement and accumulation of structural and point defects, resulting in a significant contribution of stacking faults (SFs) resulting in the destabilization of crystalline structures. As a consequence, we demonstrated that mechanical alloying is a nonequilibrium process, where phase composition and transformation of binary NiTi can be modified from that predicted using thermodynamic equilibrium phase diagram.

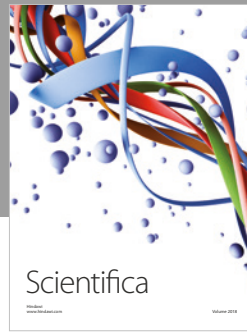
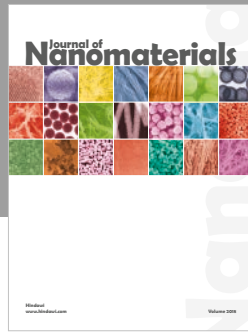
Conflicts of Interest

The authors declare that there are no conflicts of interest.

References

- [1] A. Tuissi, G. Rondelli, and P. Bassani, "Plasma Arc Melting (PAM) and Corrosion Resistance of Pure NiTi Shape Memory Alloys," *Shape Memory and Superelasticity*, vol. 1, no. 1, pp. 50–57, 2015.
- [2] J. Witkowska, J. Kaminski, T. P. Iocinski et al., "Corrosion resistance of NiTi shape memory alloy after hybrid surface treatment using low-temperature plasma," *Vacuum*, vol. 137, pp. 92–96, 2017.
- [3] C. H. Ng, R. Nanxi, W. C. Law et al., "Enhancing the cell proliferation performance of NiTi substrate by laser diffusion nitriding," *Surface Coatings Technology* 309, pp. 59–66, 2017.
- [4] J. Sevcikova and M. Pavkova Goldbergova, "Biocompatibility of NiTi alloys in the cell behaviour," *BioMetals*, vol. 30, no. 2, pp. 163–169, 2017.
- [5] R. Piquard, A. D'Acunto, P. Laheurte, and D. Dudzinski, "Micro-end milling of NiTi biomedical alloys, burr formation and phase transformation," *Precision Engineering*, vol. 38, no. 2, pp. 356–364, 2014.
- [6] S. A. Thompson, "An overview of nickel-titanium alloys used in dentistry," *International Endodontic Journal*, vol. 33, pp. 297–310, 2000.
- [7] T. Saito, T. Yokoyama, and A. Takasaki, "Hydrogenation of TiNi shape memory alloy produced by mechanical alloying," *Journal of Alloys and Compounds*, vol. 509, no. 2, pp. S779–S781, 2011.
- [8] L. A. L. Pavón, E. L. Cuellar, C. Ballesteros, A. T. Castro, A. M. De La Cruz, and C. J. De Araújo, "Nanoparticles from Cu-Zn-Al shape memory alloys physically synthesized by ion milling deposition," *Materials Research*, vol. 15, no. 3, pp. 341–346, 2012.
- [9] M. Izadinia and K. Dehghani, "Structure and properties of nano-structured Cu-13.2Al-5.1Ni shape memory alloy produced by melt spinning," *Transactions of Nonferrous Metals Society of China*, vol. 21, no. 9, pp. 2037–2043, 2011.
- [10] Q. Dai, M. Asif warsi, J. Q. Xiao, and S. Ren, "Solution processed MnBi-FeCo magnetic nanocomposites," *Nano Research*, vol. 9, no. 11, pp. 3222–3228, 2016.
- [11] K. Y. Chiu, M. H. Wong, F. T. Cheng, and H. C. Man, "Characterization and corrosion studies of titania-coated NiTi prepared by sol-gel technique and steam crystallization," *Applied Surface Science*, vol. 253, no. 16, pp. 6762–6768, 2007.
- [12] T. Mousavi, F. Karimzadeh, and M. H. Abbasi, "Synthesis and characterization of nanocrystalline NiTi intermetallic by mechanical alloying," *Materials Science and Engineering: A Structural Materials: Properties, Microstructure and Processing*, vol. 487, no. 1-2, pp. 46–51, 2008.

- [13] M. H. Elahinia, M. Hashemi, M. Tabesh, and S. B. Bhaduri, "Manufacturing and processing of NiTi implants: a review," *Progress in Materials Science*, vol. 57, no. 5, pp. 911–946, 2012.
- [14] M. Karlik, P. Haušild, M. Klementová et al., "TEM phase analysis of NiTi shape memory alloy prepared by self-propagating high-temperature synthesis," *Advances in Materials and Processing Technologies*, vol. 3, no. 1, pp. 58–69, 2016.
- [15] T. Kurita, H. Matsumoto, K. Sakamoto, and H. Abe, "Transformation behavior of shock-compressed Ni₄₈Ti₅₂," *Journal of Alloys and Compounds*, vol. 400, no. 1-2, pp. 92–95, 2005.
- [16] M. Akmal, A. Raza, M. M. Khan, M. I. Khan, and M. A. Hussain, "Effect of nano-hydroxyapatite reinforcement in mechanically alloyed NiTi composites for biomedical implant," *Materials Science and Engineering C: Materials for Biological Applications*, vol. 68, pp. 30–36, 2016.
- [17] M. Karolus and J. Panek, "Nanostructured Ni-Ti alloys obtained by mechanical synthesis and heat treatment," *Journal of Alloys and Compounds*, vol. 658, pp. 709–715, 2016.
- [18] C. Suryanarayana, "Structure and properties of ultrafine-grained MoSi₂ + Si₃N₄ composites synthesized by mechanical alloying," *Materials Science and Engineering: A Structural Materials: Properties, Microstructure and Processing*, vol. 479, no. 1-2, pp. 23–30, 2008.
- [19] R. Amini, F. Alijani, M. Ghaffari, M. Alizadeh, and A. K. Okyay, "Formation of B19', B2, and amorphous phases during mechano-synthesis of nanocrystalline NiTi intermetallics," *Powder Technology*, vol. 253, pp. 797–802, 2014.
- [20] B. Avar, "Structural, thermal and magnetic characterization of nanocrystalline Co₆₅Ti₂₅W₅B₅ powders prepared by mechanical alloying," *Journal of Non-Crystalline Solids*, vol. 432, pp. 246–253, 2016.
- [21] F. Hadeif, A. Otmani, A. Djekoun, and J. M. Grenèche, "Structural and microstructural study of nanostructured Fe₅₀Al₄₀Ni₁₀ powders produced by mechanical alloying," *Materials Characterization*, vol. 62, no. 8, pp. 751–759, 2011.
- [22] G. K. Williamson and W. H. Hall, "X-ray line broadening from filed aluminium and wolfram," *Acta Metallurgica et Materialia*, vol. 1, no. 1, pp. 22–31, 1953.
- [23] J. I. Langford, "The accuracy of cell dimensions determined by Cohen's method of least squares and the systematic indexing of powder data," *Journal of Applied Crystallography*, vol. 6, no. 3, pp. 190–196, 1973.
- [24] B. E. Warren and B. L. Averbach, "The Effect of Cold-Work Distortion on X-Ray Patterns," *Journal of Applied Physics*, vol. 21, no. 6, pp. 595–599, 1950.
- [25] H. M. Rietveld, "A profile refinement method for nuclear and magnetic structures," *Journal of Applied Crystallography*, vol. 2, pp. 65–71, 1969.
- [26] P. Pourghahramani, E. Altin, M. R. Mallebakam, W. Peukert, and E. Forssberg, "Microstructural characterization of hematite during wet and dry millings using Rietveld and XRD line profile analyses," *Powder Technology*, vol. 186, no. 1, pp. 9–21, 2008.
- [27] H. Dutta, A. Sen, J. Bhattacharjee, and S. K. Pradhan, "Preparation of ternary Ti_{0.9}Ni_{0.1}C cermets by mechanical alloying: Microstructure characterization by Rietveld method and electron microscopy," *Journal of Alloys and Compounds*, vol. 493, no. 1-2, pp. 666–671, 2010.
- [28] N. Loudjani, N. Bensebaa, L. Dekhil, S. Alleg, and J. J. Suñol, "Structural and magnetic properties of Co₅₀Ni₅₀ powder mixtures," *Journal of Magnetism and Magnetic Materials*, vol. 323, no. 23, pp. 3063–3070, 2011.
- [29] N. Loudjani, M. Benchiheub, and M. Bououdina, "Structural, Thermal and Magnetic Properties of Nanocrystalline Co₈₀Ni₂₀ Alloy Prepared by Mechanical Alloying," *Journal of Superconductivity and Novel Magnetism*, vol. 29, no. 11, pp. 2717–2726, 2016.
- [30] M. B. Makhlof, T. Bachaga, J. J. Sunol, M. Dammak, and M. Khitouni, "Synthesis and characterization of nanocrystalline Al-20 at. % Cu powders produced by mechanical alloying," *Metals*, vol. 6, no. 7, article no. 145, 2016.
- [31] M. Bortolotti, L. Lutterotti, and G. Pepponi, "Combining XRD and XRF analysis in one Rietveld-like fitting," *Powder Diffraction*, vol. 32, no. S1, pp. S225–S230, 2017.
- [32] G. Caglioti, A. Paoletti, and F. P. Ricci, "Choice of collimators for a crystal spectrometer for neutron diffraction," *Nuclear Instruments*, vol. 3, no. 4, pp. 223–228, 1958.
- [33] B. E. Warren and B. L. Averbach, "The effect of cold-work distortion on x-ray patterns," *Journal of Applied Physics*, vol. 21, no. 6, pp. 595–599, 1950.
- [34] R. J. Hill, "Expanded use of the rietveld method in studies of phase abundance in multiphase mixtures," *Powder Diffraction*, vol. 6, no. 2, pp. 74–77, 1991.
- [35] R. Amini, M. J. Hadianfard, E. Salahinejad, M. Marasi, and T. Sritharan, "Microstructural phase evaluation of high-nitrogen Fe-Cr-Mn alloy powders synthesized by the mechanical alloying process," *Journal of Materials Science*, vol. 44, no. 1, pp. 136–148, 2009.
- [36] C. Suryanarayana, "Mechanical alloying and milling," *Progress in Materials Science*, vol. 46, no. 1-2, pp. 1–184, 2001.
- [37] B.-Y. Li, L.-J. Rong, and Y.-Y. Li, "Stress-strain behavior of porous Ni-Ti shape memory intermetallics synthesized from powder sintering," *Intermetallics*, vol. 8, no. 5-6, pp. 643–646, 2000.
- [38] W. Maziarz, J. Dutkiewicz, J. Van Humbeeck, and T. Czeppe, "Mechanically alloyed and hot pressed Ni-49.7Ti alloy showing martensitic transformation," *Materials Science and Engineering: A Structural Materials: Properties, Microstructure and Processing*, vol. 375-377, no. 1-2, pp. 844–848, 2004.
- [39] T. Bachaga, R. Daly, L. Escoda, J. J. Suñol, and M. Khitouni, "Amorphization of Al₅₀(Fe₂B)₃₀Nb₂₀ mixture by mechanical alloying," *Metallurgical and Materials Transactions A: Physical Metallurgy and Materials Science*, vol. 44, no. 10, pp. 4718–4724, 2013.
- [40] J. Sort, J. Nogués, S. Suriñach, J. S. Muñoz, and M. D. Baró, "Correlation between stacking fault formation, allotropic phase transformations and magnetic properties of ball-milled cobalt," *Materials Science and Engineering: A Structural Materials: Properties, Microstructure and Processing*, vol. 375-377, no. 1-2, pp. 869–873, 2004.



Hindawi
Submit your manuscripts at
www.hindawi.com

